Variational Transition-State Theory with Optimized Orientation of the Dividing Surface and Semiclassical Tunneling Calculations for Deuterium and Muonium Kinetic Isotope Effects in the Free Radical Association Reaction $H + C_2H_4 \rightarrow C_2H_5$

Jordi Villà,[†,‡,§] José C. Corchado,[‡,||] Angels González-Lafont,[†] José M. Lluch,[†] and Donald G. Truhlar*[,‡]

Unitat de Química Física, Departament de Química, Universitat Autònoma de Barcelona, 08193 Bellaterra, Barcelona, Spain, Department of Chemistry and Supercomputer Institute, University of Minnesota, Minneapolis, Minnesota 55455-0431, Grup de Recerca en Informàtica Mèdica, Institut Municipal d'Investigació Mèdica, IMIM, Doctor Aiguader 80, 08003 Barcelona, Spain, and Departamento de Química Física, Universidad de Extremadura, 06071 Badajoz, Spain

Received: March 19, 1999; In Final Form: May 3, 1999

We have used canonical variational transition-state theory with multidimensional tunneling contributions (CVT/MT) to calculate 21 kinetic isotope effects (KIE) for the addition of hydrogen atom to ethylene. The potential energies are obtained by variable scaling of external correlation (VSEC). The reorientation of the dividing surface (RODS) algorithm is employed so that the same reaction path can be used for every isotopic substitution. The results show the importance of the tunneling effect for explaining the trends in the KIEs in this almost barrierless reaction. We have predicted the regioselectivity for three different isotopically substituted substrates and have shown how the addition to the most substituted carbon is kinetically favored, especially at low temperature. However, our calculations show no cis/trans selectivity for the isotopically substituted ethylene substrate.

1. Introduction

The addition of a hydrogen atom to ethylene constitutes the simplest radical addition to an olefin. This reaction has been extensively studied both experimentally[1−4] and theoretically.[5−10] The mechanism of the process is now well understood and can be approximately represented by the following scheme:

$$H + C_2H_4 \xrightarrow{k_1} C_2H_5^* \qquad \text{(R1)}$$

$$C_2H_5^* \xrightarrow{k_d} H + C_2H_4 \qquad \text{(R1d)}$$

$$C_2H_5^* \xrightarrow[M]{k_s} C_2H_5 \qquad \text{(R1s)}$$

where $C_2H_5^*$ is a vibrationally hot ethyl radical[11] and M is a third body. Assuming that the steady-state approximation is valid for the concentration of the vibrationally hot ethyl radicals, the apparent bimolecular rate coefficient for addition will be

$$k_{app} = \frac{k_1 k_s[M]}{k_d + k_s[M]} \qquad (1)$$

where [M] is the concentration of the third body. More realistically, one would recognize that ethyl radicals with different total energies decompose at different rates, leading to energy-dependent k_d.

Experimentally, a major difficulty in studying the addition reaction is sorting out the pressure and energy dependences and obtaining an elementary rate coefficient for each step. However, the situation becomes considerably simplified in the high-pressure limit because k_{app} reduces to k_1; furthermore, the hot radicals may be assumed to be fully equilibrated, so k_d becomes a simple function of temperature T, and $k_1(T)/k_d(T) = K(T)$, where K is the equilibrium constant for $H + C_2H_4 \rightleftharpoons C_2H_5$. There now exists a good consensus on the various experimental values for the elementary addition[1f,i,k,n,s,u,2,3] and dissociation[1d,e,q,t,v] rate coefficients $k_1(T)$ and $k_d(T)$ corresponding to this high-pressure limit, and recommended expressions for both the addition and the dissociation reactions have been proposed.[1v] The present paper will be concerned entirely with the high-pressure association rate coefficient, $k_1(T)$, and those of its isotopic derivatives, $k_2(T)$ through $k_{16}(T)$, which are enumerated in Table 1.

Radical addition reactions are difficult to study theoretically because accurate electronic structure calculations are very difficult. The difficulty results both from the low barrier found for such reactions[12] and from the difficulty of treating the radicals because of their open-shell character.[13] Theoretical studies of the title reaction have raised two major subjects of discussion: (1) whether transition-state theory (TST) and RRKM theory can simultaneously fit the rates of the $C_2H_4 + H$ addition and the C_2H_5 unimolecular dissociation; (2) whether the transition state is loose or tight. Work by Hase, Schlegel, and co-workers[7,8] seems to have answered both questions, namely, "yes" for question 1 and "loose" for question 2. They proposed a transition state with a fixed geometry for all temperatures considered (a *static* transition state), and they obtained the final rate constants using conventional transition-state theory. The potential energy barrier was fitted to reproduce the experimental

[†] Universitat Autònoma de Barcelona.
[‡] University of Minnesota.
[§] Institut Municipal d'Investigació Mèdica.
[||] Universidad de Extremadura.

10.1021/jp990970c CCC: $18.00
Published on Web 06/16/1999

TABLE 1: Reactions Considered in This Study

subject	reaction		σ
unsubstituted reaction	$^{\bullet}H + CH_2CH_2 \rightarrow {}^{\bullet}CH_2CH_3$	R1	4
primary and secondary KIEs	$^{\bullet}D + CH_2CH_2 \rightarrow {}^{\bullet}CH_2CH_2D$	R2	4
	$^{\bullet}Mu + CH_2CH_2 \rightarrow {}^{\bullet}CH_2CMuH_2$	R3	4
	$^{\bullet}H + CD_2CD_2 \rightarrow {}^{\bullet}CD_2CHD_2$	R4	4
	$^{\bullet}D + CD_2CD_2 \rightarrow {}^{\bullet}CD_2CD_3$	R5	4
	$^{\bullet}Mu + CD_2CD_2 \rightarrow {}^{\bullet}CD_2CMuD_2$	R6	4
regioselectivity	$^{\bullet}H + CD_2CHD \rightarrow {}^{\bullet}CD_2CH_2D$	R7a	2
	$^{\bullet}H + CD_2CHD \rightarrow {}^{\bullet}CHDCHD_2$	R7b	2
	$^{\bullet}H + CH_2CHD \rightarrow {}^{\bullet}CH_2CH_2D$	R8a	2
	$^{\bullet}H + CH_2CHD \rightarrow {}^{\bullet}CHDCH_3$	R8b	2
	$^{\bullet}D + CD_2CHD \rightarrow {}^{\bullet}CHDCD_3$	R9a	2
	$^{\bullet}D + CD_2CHD \rightarrow {}^{\bullet}CD_2CHD_2$	R9b	2
	$^{\bullet}D + CH_2CHD \rightarrow {}^{\bullet}CH_2CHD_2$	R10a	2
	$^{\bullet}D + CH_2CHD \rightarrow {}^{\bullet}CHDCH_2D$	R10b	2
	$^{\bullet}H + CD_2CH_2 \rightarrow {}^{\bullet}CH_2CHD_2$	R11a	2
	$^{\bullet}H + CD_2CH_2 \rightarrow {}^{\bullet}CD_2CH_3$	R11b	2
	$^{\bullet}D + CD_2CH_2 \rightarrow {}^{\bullet}CD_2CH_2D$	R12a	2
	$^{\bullet}D + CD_2CH_2 \rightarrow {}^{\bullet}CH_2CD_3$	R12b	2
stereoselectivity	$^{\bullet}H +$ *cis*-CHDCHD $\rightarrow {}^{\bullet}CHDCH_2D$	R13	4
	$^{\bullet}H +$ *trans*-CHDCHD $\rightarrow {}^{\bullet}CHDCH_2D$	R14	4
	$^{\bullet}D +$ *cis*-CHDCHD $\rightarrow {}^{\bullet}CHDCHD_2$	R15	4
	$^{\bullet}D +$ *trans*-CHDCHD $\rightarrow {}^{\bullet}CHDCHD_{22}$	R16	4

results for both the addition and the dissociation reactions. However, as pointed out in previous studies of the present authors for the title reaction[9] and for the related association reaction $C_2H_4 + OH \rightarrow C_2H_4OH$,[14] variational optimization of the location of the transition state for different temperatures (*dynamic* transition states) is crucial for understanding the looseness of addition reaction transition states and for making quantitative estimates of entropies of activation. The latter were shown to be the origin of the negative temperature dependence of the rate constant for the OH addition to ethylene.

Most of the studies on $H + C_2H_4$ have been carried out with protium atoms and the perprotio ethylene molecule;[1,5] however, much attention has also been devoted to kinetic isotope effects (KIEs). Cowfer and Michael[2] carried out room-temperature experiments for two partially deuterated versions of the reaction and the fully deuterated version, and they used theory to try to disentangle k_1 from k_{app}. In particular, they applied conventional transition-state theory in order to understand the distribution of products. They fitted the parameters needed for the calculations to the kinetic results obtained for the nondeuterated case. By assuming that the geometry, energy, and force constants of the transition state are invariant to isotopic substitution, they concluded that the experimental KIEs are due exclusively to differences in the zero-point-inclusive energy barriers of the *static* transition states given by

$$\Delta V_a^{G\ddagger} = \Delta V^{\ddagger} + \epsilon^{G\ddagger} - \epsilon^{GR} \qquad (2)$$

where $\Delta V^{\ddagger}$ is the potential energy of the saddle point relative to reactants, $\epsilon^{G\ddagger}$ is the zero-point vibrational energy of the transition state, and ϵ^{GR} is the zero-point vibrational energy of reactants.

A later study by Nagase et al.[6] employed the UHF level of electronic structure theory and conventional transition-state theory (TST). Their calculations yielded a transition-state model that fits quite accurately the experimental data of Lee et al.[1n] for the perprotio addition (Arrhenius parameters: $A^{TST} = 10^{-10.3}$ cm^3 molecule^{-1} s^{-1}vs $A^{Exp} = 10^{-10.4}$ cm^3 molecule^{-1} s^{-1}; $E_a^{TST} = 2.3$ kcal/mol vs $E_a^{Exp} = 2.1$ kcal/mol). Encouraged by this success, the authors studied the KIEs for D atoms and deuterated ethylene, including the stereo- and regioselectivity of the isotopically substituted substrates. They predicted that at low temperatures, the D addition would be faster than the H addition because of a smaller $\Delta V_a^{G\ddagger}$ for the former, while at higher temperatures the higher Arrhenius preexponential factor for the H addition would invert this behavior. They also predicted a slightly higher reactivity for the cis isotopomer in the X + CHDCHD reaction (with X = H, D) and a general preference for both H and D to add to the most deuterated carbon in the series $CHDCH_2$, CD_2CH_2, and CD_2CHD. Both of these propensities are the opposite of what occurs in olefins bearing a nonisotopic substituent.[6] In light of more experience with electronic structure theory, we now realize that electronic structure calculations without electron correlation, as employed in these pioneering studies, are not reliable,[7] and the good agreement with some of the experimental data was fortuitous.

Sugawara et al.[3] measured the high-pressure limit of several of the KIEs for the reactions of H and D with C_2H_4, $CHDCH_2$, and C_2D_4 over the temperature interval 206−461 K. They compared their results to TST calculations based on the Nagase et al.[6] transition-state model with the Wigner tunneling formula. The theoretical results differed qualitatively from the experimental ones; this was especially so for the temperature dependences, with very severe differences for the transition-state model of Cowfer and Michael and less severe but still "very poor" differences for the Nagase et al. parameters. The former problem was attributed to a 120 cm^{-1} bending frequency at the transition state in the Cowfer−Michael model, whereas this is increased to 404 cm^{-1} in the Nagase et al. model. The errors in the calculations with the Nagase et al. model were attributed to the deficiency of conventional transition-state theory, in particular to a large amount of recrossing of the conventional transition state.

Muonium KIEs are expected to be very informative because of the extremely large mass ratio, about 8.8, of H to Mu. (A muonium atom is composed of an electron and a positive muon, which is much lighter than a proton but still heavy enough for the Born−Oppenheimer approximation to be reasonably accurate.[15]) Garner et al.[4] used the muon spin rotation method to obtain rate constants for the addition processes $Mu + C_2H_4$ and $Mu + C_2D_4$. This technique allows the "direct" measurement of the addition rate constants k_3 and k_6, independent of the pressure. When compared with the results of Sugawara et al.,[3] the data of Garner et al. show very large increases in the rate constants, with the ratios k_3:k_1:k_2 being approximately 4.0:1.4:1.0 at ∼500 K and 70.:1.4:1.0 at ∼150 K. The study of Garner et al. suggests that the rate increase for Mu might be explained by tunneling through a loose, early transition state. This implies that the effects of zero-point energy are less important than assumed previously and that translational energy is mainly responsible for promoting the reaction.

In previous studies we have shown how the inclusion of multidimensional tunneling effects accounts quantitatively for the curvature of the Arrhenius plots in the $Mu + C_2H_4$,[10] $H + C_2H_4$,[9,10] and $D + C_2H_4$ reactions.[10] The objective of the present paper is to examine the roles of variational location of the dynamical bottleneck and multidimensional tunneling for the whole range of primary and secondary KIEs of the title reaction. This should allow us to obtain a much more complete picture of this system, which is the simplest prototype for the kinetics of radical additions to olefins and hence of great fundamental interest. Table 1 lists the 22 different reactions considered in this work.

To obtain a reliable potential energy profile for the dynamics study, we have introduced[9] a new way to extrapolate electronic structure calculations to the limit of full configuration mixing

and a complete electron basis. This method, called variable scaling of external correlation (VSEC), is based on the previously described scaled external correlation method (SEC).[16] It uses a geometry-dependent scale factor to combine a complete active space self-consistent field (CASSCF) calculation with a calculation that includes an appreciable amount of the dynamical correlation energy. The new method, combined with variational transition-state theory[17] (VTST), allowed us to obtain realistic potential energy surface information for direct dynamics[18] calculations of the perprotio title reaction[9] and also the D and Mu additions to the unsubstituted substrate.[10]

The first step in traditional methods for computing VTST rate coefficients and multidimensional semiclassical tunneling probabilities is to calculate the minimum energy path (MEP),[19−21] which is defined as the paths of steepest descent from the saddle point to reactants and from the saddle point to products, as calculated in an isoinertial coordinate system. (An isoinertial coordinate system is any coordinate system in which the same reduced mass is used for all possible directions of motion. The MEP in isoinertial coordinates[19,20] is also called[21] the "intrinsic" reaction path.) The signed arc length along the MEP is called the scalar reaction coordinate *s*. By definition the MEP depends on the atomic masses of the atoms involved in the reaction, and therefore, a new MEP should be calculated for each isotopic substitution. However, under the Born−Oppenheimer approximation, the potential energy surface for a system depends on the atomic numbers but not on the masses of the nuclei involved in a reaction. To take advantage of this, new methods[22,23] have been developed for computing VTST reaction rate constants including multidimensional tunneling contributions without having to evaluate the MEP at all or without having to evaluate a new one for each isotopically substituted reaction. These new methods have been successfully applied to the calculation of reaction rates for several reactions.[9,10,22−24] Therefore, only one reaction path needs to be constructed, and it may be an MEP for the isotopically unsubstituted reaction or it may be a distinguished-coordinate[25] path (DCP), which is independent of masses. In the present paper we use the latter choice.

2. Methods and Calculations

2.1. Electronic Structure Calculations. Geometries, energies, and first and second energy derivatives were calculated using the *Gaussian 94* program.[26] We recall that the general notation X//Y[27] denotes geometry optimization and Hessian evaluation (for frequencies) at level Y followed by a single-point energy calculation at level X. As usual, we omit //Y if Y is the same as X. A consequence of this standard notation is that by default X//Y calculations involve a level-Y Hessian, whereas a level-X Hessian is the default for X calculations. As usual,[27] X and Y each has the form L/B, where L denotes the Hartree−Fock or correlation level (i.e., the many-electron level) and B denotes the one-electron basis.

Figure 1 shows the definitions of internal coordinates for the stationary-point geometries in the system. Stationary-point geometries (reactants, product, and saddle point) for reaction R1 were optimized, and the harmonic vibrational frequencies were calculated using quadratic configuration interaction with single and double excitations[28] (QCISD) and the 6-311G(d,p) basis set.[27] Previous work[9,10] showed that this provides an adequate basis for applying the VSEC method (see below) to obtain quantitatively accurate results in the dynamical study of reaction R1 and its reverse process.

To obtain reliable thermochemical properties for the addition processes, we have also performed a calculation using the new

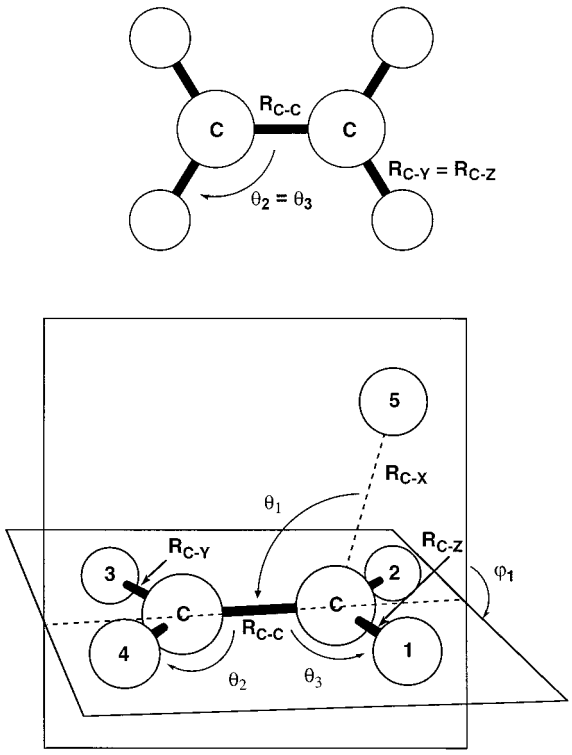

Figure 1. Definition of the geometrical parameters in Table 2 and Figures 2 and 3.

complete basis set method (CBS-RAD) that was specifically designed for radicals by Mayer et al.[13]

A DCP has been constructed by fixing the R_{C-X} distance (see Figure 1) at different values and allowing the other degrees of freedom to relax. In this way, we calculated 13 points along the DCP on the reactant side of the saddle point and 8 along the DCP on the product side. At the QCISD/6-311G(d,p) level these points cover the interval $R_{C-X} = [1.5$ Å, 2.9 Å$]$. The DCP points are more concentrated around the saddle point than far from it because this is where the variational transition states are expected to be located and where tunneling is more likely to occur. The energy of these points will be called V_{DCP}.

At each DCP geometry j (with $j = 1, 2, ..., 21$), a generalized normal-mode analysis[29] in redundant internal coordinates[30] has been performed using a QCISD/6-311G(d,p) Hessian. (The internal coordinates are curvilinear, which means the generalized-transition-state dividing surface is curved, which is more physical than a hyperplane in Cartesian coordinates.) By diagonalizing the Hessian with one direction projected out[30−32] at each DCP point, we obtain the $3N - 7 = 14$ (where N is the number of atoms of the system) eigenvectors $\mathbf{L}_m^{GT}(j)$ corresponding to the generalized normal-mode motions orthogonal to the path and their corresponding eigenvalues. The latter provide the generalized frequencies $\omega_m(j)$ along the path (where m labels one of the 14 generalized normal modes). Since an MEP was not calculated, projecting out the frequencies by projecting the local gradient[31] obtained from the DCP optimizations may lead to unphysical results.[22−24] Since MEP calculations are known from experience[17,20,32−35] to lead to physical reaction-path frequencies, this may be explained by the fact that, in general, the DCP geometry does not lie on the MEP, and for this reason the gradients obtained from the DCP calculation are not parallel to the gradients one could obtain from an MEP calculation. Thus, the recently developed RODS algorithm,[22] in which the projected direction (which would be taken as the gradient $\mathbf{g}(j)$ in a typical MEP calculation) is variationally

optimized (obtaining an optimized direction $\mathbf{v}(j)$), has been applied to obtain physical eigenvectors and generalized frequencies along the DCP path by maximizing the generalized free energy of activation at 0 K for each point j. The resulting $\omega_m(j)$ values are used to calculate the vibrationally adiabatic ground-state potential energy curve $V_a^G(j)$. This is defined, at each DCP point j, by[22]

$$V_a^G(j) = V_M(j) + \frac{1}{2}\hbar \sum_{m=1}^{3N-7} \omega_m(j) \tag{3}$$

where V_M is the minimum energy in the RODS dividing surface at point j [$V_M(j) \leq V_{DCP}(j)$]. The determination of V_M is described elsewhere.[22]

Finally, at each DCP point, and also at the stationary points, several single-point energy corrections using the same 6-311G(d,p) basis set have been computed, namely, the following: (a) quadratic configuration interaction with single and double excitations and a quasiperturbative estimate of the effect of connected triple excitations[28] coupled to both single and double excitations (QCISD(T)); (b) coupled cluster with single and double excitations[36] (CCSD) with the same kind of quasiperturbative estimate of the effect of connected triple excitations[37] (CCSD(T)); (c) complete active space multiconfiguration SCF[38] (CASSCF) using three electrons in three orbitals as in the previous work;[9,10] (d) second-order perturbation theory based on the CASSCF state as a reference state[39] (CASSCF-MP2). The QCISD(T), CCSD, and CCSD(T) calculations are based on an unrestricted Hartree−Fock reference state.

2.2. Reaction Coordinate *s*. To variationally optimize the transition-state geometry and to apply tunneling corrections with the methods we will describe below, we need to map the RODS-optimized DCP points j onto a reaction coordinate s. This s is taken as the signed distance in mass-scaled coordinates[17,20] along the sequence of RODS-optimized points from the saddle point (positive on the product side and negative on the reactant side). In all cases the coordinates were scaled to a mass of 1 amu. To calculate the distance between two consecutive points $j_a = i$ and $j_b = i + 1$, we first ensure that the orientation of the molecular system is consistent. This is accomplished by using the algorithm proposed by Chen,[40] which involves rotating the Cartesian coordinates of point j_b in order to obtain a minimum distance in mass-scaled coordinates between the two points. This method also yields rotation matrices along the reaction path that are used for ensuring that other reaction path quantities (gradients and Hessians) are consistently aligned for each point along the reaction path.

Because the Born−Oppenheimer approximation is assumed to be valid, the potential energy surface does not depend on the masses of the atoms. However, the reaction path, the value of s, the moments of inertia, and the frequencies and curvature of the reaction path do depend on the masses of the atoms. Nevertheless, with the algorithms used here, no extra electronic structure calculations are needed for various isotopic substitutions. Although the same DCP points are used for every new isotopic substitution, the RODS algorithm is reapplied for each one of them.[23]

2.3. Dynamical Calculations. The first-level reaction-path information (DCP geometries, optimized RODS geometries and directions $\mathbf{v}(s)$, and energy second derivatives, all of them calculated using the same molecular orientation or transformed to the same orientation) and the higher-level single-point energies along the first-level path are used to calculate high-pressure association rate constants as functions of temperature. These calculations are carried out by canonical variational transition-state theory[17,41] (CVT) with multidimensional tunneling corrections[33−35] (MT), and the rate constants are denoted $k(T)^{CVT/MT}$. The CVT method involves calculating the standard-state generalized-transition-state (GT) free energy of activation profile defined by

$$\Delta G^{GT,0}(T,s) = RT\left[\frac{V_M(s)}{k_B T} - \ln\frac{Q^{GT}(T,s)}{\Phi^R(T)K^0}\right] \tag{4}$$

where R is the gas constant, k_B is the Boltzmann constant, $Q^{GT}(T,s)$ is the partition function for a generalized transition state at a distance s along the DCP from the saddle point as defined above, K^0, in cm^3 molecule^{-1}, is the reciprocal of the standard-state concentration, and $\Phi^R(T)$ is the reactant partition function per unit volume. Note that $V_M(s)$ depends on masses because the RODS path depends on masses. The vibrational and rotational contributions to the free energy also depend on masses. For each mass combination, the variational transition state is optimized by finding the value $s = s_*(T)$ at which $\Delta G^{GT,0}(T,s)$ is a maximum, and the CVT rate coefficient is defined by

$$k^{CVT}(T) = \frac{k_B T}{h} K^0 \min_s \left\{\sigma(s)\exp\left[-\frac{\Delta G^{GT,0}(T,s)}{k_B T}\right]\right\} \tag{5}$$

where $\sigma(s)$ is the reaction path symmetry factor, which accounts for the number of equivalent reaction paths. (Note that all the symmetry numbers are omitted in eq 4.)

In general,[42]

$$\sigma(s) = \frac{n\sigma^R}{\sigma^{GT}(s)} \tag{6}$$

where n is the number of identical transition states, σ^R is the usual rotational symmetry number for the reactants (it would be the product of these symmetry numbers if there were two molecular reactants, but in the present case one reactant is an atom), and $\sigma^{GT}(s)$ is the usual rotational symmetry number for the generalized transition state at s. In our applications, as usual, σ^{GT} is independent of s; thus, $\sigma(s)$ becomes a constant σ.

In the perprotio reaction, the symmetry point groups for reactants and transition state are D_{2h} and C_s, respectively, with symmetry numbers 4 and 1,[43] and $n = 1$, yielding $\sigma = 4$ for the addition process in R1. This agrees with our intuitive notation that there are four reaction paths corresponding to top-side and bottom-side addition to both the left and right side of ethylene. For X + $CH_2CHD \rightarrow CH_2CHDX$, with X = H, D, or Mu, the point groups are C_s for reactants and C_1 for the transition state, respectively, leading to[42] $\sigma^R = 1$ and $\sigma^{GT} = 1$. In this case though, $n = 2$ because the transition state is chiral and has an optical isomer. (The case of X = H deserves a comment; ordinarily one would not expect a CH_2XY center to be a center of chirality, but the two C−H bonds at the addition center are very different at the transition state.) Therefore, $\sigma = 2$. Again, this is intuitively reasonable, since X can add from the top or bottom. Identical considerations apply to the transition state for X + *cis*-CHDCHD, so $\sigma^{GT} = 1$, $n = 2$, but now the reactant is C_{2v}, so $\sigma^R = 2$ and $\sigma = 4$. For X + *trans*-CHDCHD, the reactant has C_{2h} symmetry, so $\sigma^R = 2$, $\sigma^{GT} = 1$, $n = 2$, and so $\sigma = 4$. For X + CH_2CD_2, the reactant has C_{2v} symmetry, and we have $\sigma^R = 2$, $\sigma^{GT} = 1$, $n = 1$, so again, $\sigma = 2$. Table 1 gives the symmetry factors for each of the association reactions studied in this work.

Tunneling corrections are included as a multiplicative factor, called the ground-state multidimensional tunneling (MT) transmission coefficient $\kappa^{MT}(T)$,

$$k^{CVT/MT}(T) = \kappa^{MT}(T)k^{CVT}(T) \tag{7}$$

We consider two levels of tunneling corrections in this work, namely, zero-curvature tunneling[19,32] (ZCT) and centrifugal-dominant small-curvature tunneling[34,35] (SCT). To calculate the SCT tunneling probability, we need the reaction-path curvature at s for each mode m. The components[31] $B_{mF}(s)$ of the curvature vector are computed from the generalized normal-mode eigenvectors $\mathbf{L}_m(s)$, along with the RODS direction $\mathbf{v}(s)$, as follows:[24]

$$B_{mF}(s) = -[\sin(s)]\sum_{i=1}^{3N}\frac{d\nu_i(s)}{ds}L_{i,m}^{GT}(s) \tag{8}$$

In eq 4 for $\Delta G^{GT,0}(T,s)$, rotations are treated by the classical rigid rotor approximation, and vibrations are treated as quantum mechanical separable harmonic oscillators, except for the lowest normal mode in the C_2H_5 generalized transition states and product, corresponding to rotation about the C−C bond, which is treated with the hindered rotor[44] approximation. To obtain the properties required for the CVT calculation (i.e., energy, frequencies, determinant of moment of inertia tensor for overall rotation, reduced moment of inertia of the hindered rotor, and reaction-path curvature components) as continuous functions of the parameter s, we interpolated the values obtained at the 21 + 3 (nonstationary plus stationary) points on the reaction path using the interpolated-VTST-by-mapping algorithm.[45]

All dynamical calculations were carried out using a modified version of the Polyrate code, version 7.9.[46]

2.4. VSEC Calculation. If the single-point energies computed at the various electron-correlation levels are used directly, the agreement of the calculated rate constants with the experimental results is very poor[9,10] because of the failure of standard ab initio methods to predict reliable potential energy surfaces for radical addition reactions.[8−10,12−14] To obtain a potential energy surface that is useful for our KIE calculations, we have used the recently developed[9] VSEC procedure. The basis of this method is the scaled external correlation (SEC) method,[16] which is based on combining the results of two ab initio calculations: a CASSCF calculation that accounts for internal (also called static) electron correlation effects and a multireference configuration interaction[47] (MRCI) that accounts for an appreciable fraction of the external (or dynamical) correlation. Then, in the SEC method, the accurate energy is approximated by

$$E_{SEC} = E_{CASSCF} + \frac{E_{MRCI} - E_{CASSCF}}{F} \tag{9}$$

where we assume that the internal correlation is correctly introduced by the CASSCF term[38,47] and that the fraction of the dynamical correlation energy recovered by the MRCI calculation with a given basis set can be represented by a constant F.[16] The VSEC approach considers this F to be a function of some distinguished coordinate, R_{C-X} in this work, that indicates the degree of progress in a direction at least approximately parallel to the reaction path. The functional form used here is the same as in ref 10 and is a slight modification of the methodology described in ref 9. It is based on the bond energy−bond order (BEBO) scheme:[48]

$$F(R_{C-X}) = F_0 + F_1 \exp\left(-\frac{R_{C-X} - R_{C-X,e}}{\gamma}\right) \tag{10}$$

where F_0 and F_1 are adjustable unitless parameters, γ is an adjustable parameter with units of length, R_{C-X} is defined in Figure 1, and $R_{C-X,e}$ is the R_{C-X} distance at the QCISD/6-311G-(d,p) C_2H_5 equilibrium geometry ($R_{C-X,e} = 1.103$ Å). The choice of an exponential, rather than say a Gaussian, is based on the fact that the valence energy varies exponentially with distance along a bond-making coordinate.[49] At the $C_2H_4 + H$ reactant structure, R_{C-X} is equal to infinity, so F for reactants is F_0. Analogously, at the C_2H_5 product (P) structure, eq 10 reduces to $F_0 + F_1$ for products.

In ref 9, the MRCI method,[50] which was used in the original SEC theory but which is not size-consistent, was replaced by a QCISD(T) calculation. For some systems CCSD(T) calculations have been found to be more reliable than QCISD(T),[51] and for this reason we switched from QCISD(T) to CCSD(T) for the DCP calculations in ref 10 and the present work. A second way in which the present work and ref 10 differs from ref 9 is that we calculated the DCP geometries at the QCISD level rather than the MP2 level (the reason for this is discussed in section 3.1). A third difference from ref 9 is the procedure for obtaining the three parameters needed in eq 10. In ref 9, the parameters were varied manually until good agreement with experimental results was obtained. Now, a genetic algorithm[52,53] is used instead. The fitness function for the genetic algorithm calculation has been chosen to be of a very simple form:

$$\text{fitness} = -\left\{\frac{\sqrt{\sum_{i=1}^{n_1}\{\ln[k_1^{exp}(T_i)] - \ln[k_1^{CVT/MT}(T_i)]\}^2}}{\frac{n_1}{2}} + \frac{\sqrt{\sum_{i=1}^{n_d}\{\ln[k_d^{exp}(T_i)] - \ln[k_d^{CVT/MT}(T_i)]\}^2}}{\frac{n_d}{2}}\right\} \tag{11}$$

where n_1 and n_d are the number of experimental data for $k_1(T)$ and $k_d(T)$ used in this work and are equal to 27 and 14, respectively. We note that F_1 in eq 10 is the difference in the fraction of external correlation energy recovered by the CCSD-(T)/6-311G(d,p) calculation of the reactants and the products, which is related to the value calculated for classical potential energy difference ΔV of the products with respect to reactants, which, in turn, strongly affects the calculated equilibrium constant for the addition reaction. For convenience then, the adjustable parameters in the genetic algorithm are taken as γ, F_0, and the classical energy of reaction ΔV rather than γ, F_0, and F_1. The three parameters are adjusted to simultaneously reproduce the high-pressure experimental rate constants for the addition and the unimolecular dissociation, the ratio of which is the equilibrium constant. This procedure allows us to get a consistent energy profile that will be used for calculating the various isotope effects in reaction R1.

3. Results and Discussion

3.1. Electronic Structure Calculations without Scaling. In Table 2 we present the structural parameters obtained for the

TABLE 2: Geometries (Distances in Å and Angles in degs) Calculated by QCISD/6-311G(d,p) Method

		QCISD/6-311G(d,p)		
coordinate[a]	exptl[b] C_2H_4	C_2H_4	saddle point	C_2H_5
R_{CC}	1.339	1.339	1.353	1.499
R_{C-X}			1.976	1.103
R_{C-Y}	1.085	1.087	1.087	1.086
R_{C-Z}	1.085	1.087	1.087	1.096
θ_1			106.7	111.6
θ_2	121.1	121.6	121.4	120.5
θ_3	121.1	121.6	121.1	111.3

[a] See definitions in Figure 1. [b] Reference 54.

stationary points of the reaction at the QCISD/6-311G(d,p) level of theory. The agreement with previous calculations[8,9] and experimental[54] values (where available) is good. For the ethyl radical, the calculations reflect the expected lengthening of the R_{C-C} distance, and the R_{C-X} and R_{C-Z} distances are clearly longer than R_{C-Y}, which maintains a value close to the one it has in ethylene. In the saddle point structure, the C_2H_4 moiety resembles ethylene, with R_{C-C} only 0.014 Å longer than in reactants. The distance R_{C-X} of the attacking hydrogen from the attached carbon is 1.976 Å, which is consistent with the early character of the transition state for this reaction, as we noted in our previous work.[9]

The first six rows of Table 3 summarize the results for the energetics calculated without scaling. (The last row of this table will be explained in section 3.2.) The quantity ΔV is the classical energy of the reaction, i.e., the potential energy of the ethyl radical with respect to the reactants at infinite separation. The first row gives the results we obtained by the complete basis set method for radicals[13] (CBS-RAD), which will be used as a standard for testing the methods that are more practical for dynamics. The values computed at the CASSCF level underestimates ΔV. Since CASSCF includes internal (static) correlation energy, but a negligible portion of the external (dynamic) correlation, we conclude that the latter changes very appreciably over the course of the reaction. CASSCF-MP2 and QCISD include dynamical correlation energy and yield more accurate results, but they are still not quantitatively accurate. The single-point energy calculations performed at QCISD(T) and CCSD(T) levels, which each includes two quasiperturbative triple excitation terms, do not differ significantly from the value computed with the CBS-RAD level.

The forward and reverse potential energy barriers at different levels are also given in Table 3. The QCISD/6-311G(d,p) value corresponds to the energy of the optimized saddle point at that level of calculation. In all cases we carried out energy calculations at this structure, and these are given in the V^{SP} columns. For L = QCISD(T), CCSD(T), CASSCF(3,3), and CASSCF(3,3)-MP2, we also calculated the maximum energy

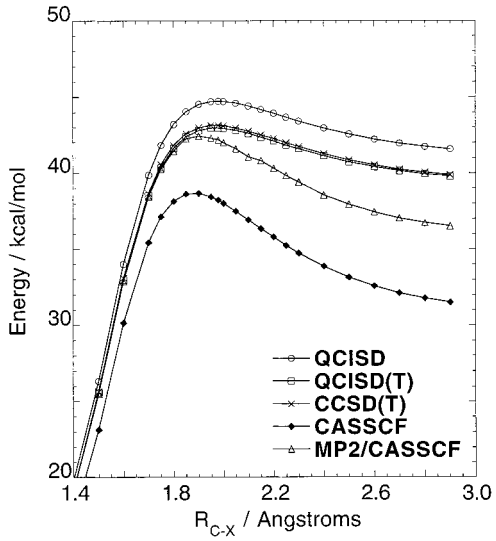

Figure 2. Potential energy profiles along the QCISD/6-311G(d,p) distinguished-coordinate path at various levels of theory for the C_2H_4 + H reaction vs the R_{C-X} distance. The basis set is 6-311G(d,p) for all these calculations.

at the L/6-311G(d,p)//QCISD/6-311G(d,p) level along the QCISD/6-311G(d,p) DCP. Although the CBS-RAD method is not designed for barrier heights, and this result must be taken with caution, the value obtained at this level for the potential energy surface is clearly below the values obtained with the above-mentioned methods.

In Figure 2, the potential energy profiles on the QCISD/6-311G(d,p) DCP at different levels of theory are plotted versus the R_{C-X} distance. Note that R_{C-X} distance decreases as the system goes from reactants to products. Thus, in Figure 2, as in all the plots versus the R_{C-X} distance in this article, the products are on the left-hand side and the reactants are on the right. From Figure 2 it is clear that the position of the maximum energy along the reaction path is dependent on the level of calculation. Thus, the lower is the calculated potential energy barrier for the addition, the larger is the value of R_{C-X} at the maximum of the curve. At the QCISD level, for example, R_{C-X} = 1.976 Å at the maximum of the potential energy profile, while at the CASSCF level it is R_{C-X} = 1.904 Å. This is consistent with the Hammond postulate,[55] and it shows how dangerous it is to use only single-point calculations at an optimized saddle point structure for reactions with flat potential energy surfaces. In the case of the CBS-RAD calculation, the maximum of the CBS-RAD//QCISD/6-311G(d,p) potential energy profile is expected to be at R_{C-X} > 1.976 Å, with a somewhat higher value for the energy barrier than the 1.32 kcal/mol calculation reported in Table 3, which is based on the QCISD/6-311G(d,p) saddle point geometry.

TABLE 3: Energetics (kcal/mol) for the C_2H_4 + H → C_2H_5 Reaction[a,b]

method	ΔV	$V^{\ddagger}$	V^{SP}	$V^{\ddagger} - \Delta V$	$V^{SP} - \Delta V$
CBS-RAD//QCISD/6-311G(d,p)	−39.57 (-33.90)		1.32 (2.99)		40.89 (36.89)
QCISD/6-311G(d,p)	−41.13	3.60	3.60	44.73	44.73
CASSCF(3,3)/6-311G(d,p)//QCISD/6-311G(d,p)	−30.72	8.38	7.94	38.65	38.21
CASSCF(3,3)-MP2/6-311G(d,p)//QCISD/6-311G(d,p)	−35.94	6.75	6.50	42.43	42.18
QCISD(T)/6-311G(d,p)//QCISD/6-311G(d,p)	−39.36	3.61	3.61	42.97	42.97
CCSD(T)/6-311G(d,p)//QCISD/6-311G(d,p)	−39.39	3.75	3.75	43.14	43.14
VSEC//QCISD/6-311G(d,p)	−40.18 (−34.60)	1.72 (2.58)[c]	1.60 (2.50)	41.90 (37.18)	41.78 (37.19)

[a] ΔV is the classical energy of reaction. $V^{\ddagger}$ and V^{SP} represent two different ways to estimate the classical barrier height. The quantity $V^{\ddagger}$ is the maximum of the curve of high-level single-point energy calculations along the DCP, which is calculated at the QCISD/6-311G(d,p) level. The V^{SP} values are high-level single-point energy calculations at the QCISD/6-311G(d,p) saddle point. [b] Values in parentheses are zero-point-energy-inclusive values (with zero-point energy calculated at the QCISD/6-31G(d) harmonic level scaled by a factor of 0.9776 for CBS-RAD and at the unscaled QCISD/6-311G(d,p) harmonic level for VSEC calculations. [c] s = −0.084 Å, where R_{C-X} = 2.055 Å and the zero-point energy is 32.86 kcal/mol.

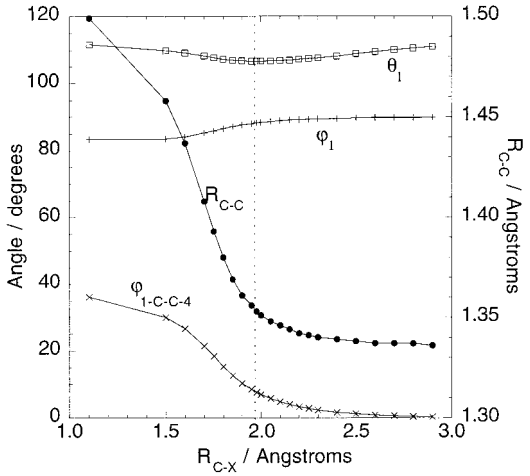

Figure 3. Evolution of several geometrical parameters along the DCP vs the R_{C-X} distance.

In Figure 3 several internal coordinates along the QCISD/6-311G(d,p) DCP have been plotted versus R_{C-X}. The vertical dotted line indicates the position of the QCISD/6-311G(d,p) saddle point. The angle between the attacking hydrogen and the two carbons of ethylene, θ_1, remains almost constant as the reaction takes place. Since the system retains C_s symmetry all along the DCP, the angle φ_1 corresponds to both the torsions 5-C−C-4 and 5-C−C-3 (see Figure 1) and indicates the development of nonplanarity at the carbon that retains sp^2 hybridization in the ethyl radical. This sp^2 carbon stays almost planar during the reaction, and φ_1 changes only slightly from its initial value of 90°. More significant effects can be seen in the evolution of the other two internal coordinates in Figure 3. Still reading from right to left, we see that the R_{C-C} distance remains almost constant until the saddle point. Then, a dramatic change occurs in the internal coordinates related to the C−C bond. On one hand, the R_{C-C} distance increases rapidly until it reaches its ethyl radical value. Simultaneously, the nonplanarity of the environment of the carbon that is attacked, represented in Figure 3 by the angle $\varphi_{1-C-C-4}$, increases rapidly. Figure 3 shows that the energy barrier for the addition process occurs very early in the process of making the C−C double bond.

In Figure 4 the expectation value of the S^2 operator, $\langle S^2 \rangle$, is plotted along the DCP. The value of $\langle S^2 \rangle$ along the DCP exceeds the value corresponding to a doublet, which is 0.75, because of contamination from higher multiplicity states. This spin contamination is the reason that we have used the QCISD method as the lower level in the present paper; in particular, experience has shown[56] that QCISD is less sensitive to spin contamination than the Møller−Plesset second-order perturbation theory (MP2) used in ref 9.

3.2. VSEC Calculations. Figure 4 also shows the Euclidean norm of the t_1 vector of the coupled-cluster wave function, denoted $||t_1||$. A value of $||t_1||$ higher than 0.02 has been proposed[57] as an indicator of the need for a multireference electron correlation procedure. Figure 4 shows that this diagnostic does exceed 0.02 over the critical part of the reaction path for our reaction. However, the MRCI calculations carried out by Hase et al.[8] on this system gave essentially the same result as the calculations at the QCISD(T) level. Because the energy barrier predicted by MRCI calculations was too high, they were unable to predict the reaction rates for the perprotio title reaction. Similarly, all of our ab initio calculations overestimate the barrier height, as can be seen in Figure 2 and Table 3. If any of the potential energy curves shown in Figure 2 are used to calculate the rate constants for the title reaction,

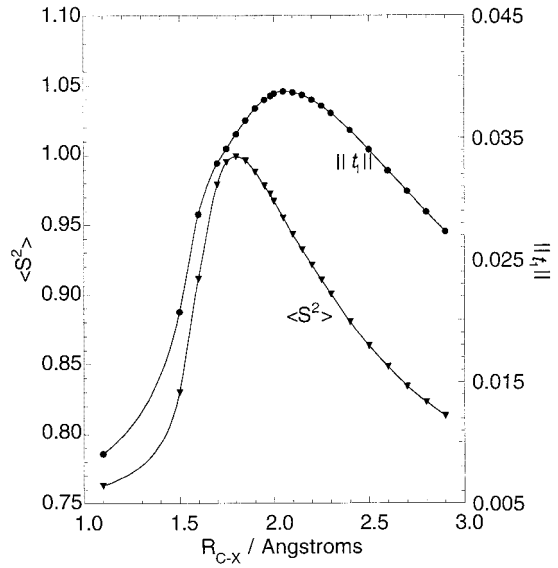

Figure 4. Evolution of the expected value of the S^2 operator, $\langle S^2 \rangle$, and of the Euclidean norm of the t_1 vector of the coupled-cluster wave function, T_1, along the DCP vs the R_{C-X} distance.

the computed values do not match the experimental results; the calculated rates are much too low. The main reason for this failure is that the ab initio barrier heights for the addition reaction are too high. In our previous work,[9] we developed the new VSEC technique for obtaining reliable potential energy surfaces for addition reactions, as outlined in section 2.4. The VSEC energy profile is obtained from eqs 9 and 10.

By use of a genetic algorithm to maximize the fitness shown in eq 10, the final parameters for the VSEC calculation in eq 9 are $F_0 = 0.6243$, $\gamma = 0.1801$ Å, and $\Delta V = -40.18$ kcal/mol. From these values, one can easily calculate that $F_1 = 8.74 \times 10^{-3}$. In the last row of Table 3, the VSEC values for the classical energy of the reaction and the energy barriers for the addition and dissociation reactions are given. The classical energy of the reaction obtained from the VSEC calculation that fits the best the experimental rate constants is in quite good agreement (0.6 kcal/mol) with the CBS-RAD calculation. The barrier heights are also remarkably similar, but this is less meaningful, since the CBS-RAD value for the energy barrier was calculated at the QCISD/6-311G(d,p) saddle point structure, which corresponds to a shorter R_{C-X} distance ($R_{C-X} = 1.976$ Å) than the corresponding R_{C-X} distance at the maximum of the potential energy profile of the VSEC calculation ($R_{C-X} = 2.07$ Å). (Recall that zero-point energeis are calculated in the harmonic approximation in this paper.)

The vibrationally adiabatic barrier height obtained for reaction R1 in the present study is 2.63 kcal/mol (at $s = -0.042$ Å where $R_{C-X} = 2.017$ Å, the potential energy is 1.69 kcal/mol and the zero-point energy is 32.94 kcal/mol, compared to the reactant zero-point energy of 32.00 kcal/mol). This may be compared to 2.70 kcal/mol obtained in ref 8 and to 2.58 kcal/mol in the present study at the saddle point (which occurs at $s = -0.084$ Å). (Recall that zero-point energies are calculated in the harmonic approximation in this paper.)

3.3. Dynamical Calculations. The first point we wish to discuss is the difference between canonical variational theory (CVT) and conventional TST, with the latter based on the location ($s = 0$) of the maximum of the lower-level QCISD/6-311G(d,p) potential energy along the original DCP (in the notation of Table 3, this is the SP version of TST, not the ‡ version). Table 4 gives the ratio of k^{TST} to k^{CVT} for three sample

TABLE 4: k^{SP}/k^{CVT} and $k^{‡}/k^{CVT}$ [a]

method	T (K)	R1[b]	R11a[b]	R12[b]
SP	200	1.05	1.05	1.24
	500	1.01	1.03	1.05
	1000	1.08	1.11	1.08
‡	200	1.21	1.20	1.00
	500	1.27	1.30	1.13
	1000	1.44	1.47	1.29

[a] k^{SP} is k^{TST} calculated using a transition-state dividing surface at the saddle point of the lower-level (QCISD) electronic structure calculation, whereas $k^{‡}$ is k^{TST} calculated using a transition-state dividing surface at the highest-energy point (obtained by interpolation) of the higher-level (QCISD(T)) energy profile along the lower-level reaction path. [b] These column headings are explained in Table 1.

TABLE 5: Value of s and R_{C-X} (in Å) at Canonical Variational Transition State

variable	T (K)	R1[a]	R11a[a]	R12b[a]
s	0	−0.042	−0.043	−0.110
	200	−0.032	−0.032	−0.104
	500	0.023	0.031	0.028
	1000	0.058	0.063	0.043
R_{C-X}	0	2.017	2.016	2.055
	200	2.007	2.006	2.050
	500	1.954	1.949	1.956
	1000	1.922	1.920	1.945

[a] These column headings are explained in Table 1.

reactions. This ratio measures the amount of recrossing of the transition state that is eliminated by moving the transition-state dividing surface from its conventional location on the basis of single-level calculations to the variationally optimized dual-level location at each temperature. The ratio is as large as 1.24 at 200 K and as large as 1.11 at 1000 K, but it is closer to unity at 500 K. Furthermore, the ratio depends on temperature and on the nature of the isotope substitution.

Although the k^{SP}/k^{CVT} ratios discussed in the previous paragraph are interesting from a practical standpoint, we also see that $k^{‡}/k^{SP} = 0.8-1.3$, where $k^{‡}$ is our best estimate of the conventional transition-state theory rate coefficient. This factor is significant, since it means that $k^{‡}/k^{CVT}$ differs from k^{SP}/k^{CVT} by this amount. The $k^{‡}/k^{CVT}$ ratios have a more fundamental significance because they measure the amount of recrossing that can be minimized by improving the dynamical formulation. These ratios are shown in the lower section of Table 4. These results again show strong isotopic dependence. Recrossing of the conventional transition state increases with temperature, up to a factor of 1.3−1.5 at 1000 K.

Table 5 shows the values of s at the canonical variational transition states for the same three reactions that were included in Table 4. This table shows that the locations of the variational transition states depend systematically on temperature, becoming tighter as T increases. The bottom half of Table 5 gives the corresponding C−X distances (see Figure 1), obtained by quartic interpolation from the output grid. We see a tightening of 0.09−0.11 Å in this critical distance. In contrast to the values in Table 5, the maxima of V_{MEP} (as used to calculate $k^{‡}$) occur at $R_{C-X} = 2.06$ Å. Thus, the dynamical bottleneck may have a C−X distance as much as 0.14 Å shorter than the saddle point. This illustrates that saddle point calculations alone are insufficient for a full understanding of the dynamics of association reactions such as the one studied here.

The localized dynamical bottleneck locations of the previous paragraph are most appropriate for characterizing the overbarrier process (where "overbarrier process" refers to the reactive flux coming from energies high enough that tunneling need not be involved). The transmission coefficients indicate the increase in the rate coefficient, relative to the contribution from the overbarrier process, that is caused by tunneling. (They also include the decrease due to nonclassical reflection, which cancels a part of the increase due to tunneling.) Table 6 shows some values of the transmission coefficient. The rate enhancement by tunneling can be more than a factor of 2 at 200 K and depends strongly on isotope.

TABLE 6: κ^{SCT}

T (K)	R1[a]	R11a[a]	R12b[a]
200	2.41	2.36	1.68
500	1.15	1.14	1.09
1000	1.03	1.03	1.02

[a] These column headings identify reactions in Table 1.

3.4. Kinetic Isotope Effects. In the following paragraphs, except in the discussion of the rule of the geometric mean, the KIEs are defined as the ratio k_i/k_j, where k_j represents the rate coefficient for the isotopic substitution with greater mass and k_i represents the rate coefficient for the corresponding lighter reaction. By definition, a KIE is "normal" if it shows a faster reaction for the lighter isotope (and therefore, the KIE is larger than unity) and it is "inverse" if the faster reaction occurs in the heavier isotopically substituted system. For cases where no confusion can result, we use H, D, and Mu as the subscripts i and j. For multiple substitution or to be perfectly unambiguous, we use the reaction numbers in Table 1.

3.4.1. Primary Kinetic Isotope Effects. Table 7 presents the results for the primary KIEs for the addition $X + C_2H_4$, with X = H, D and Mu (which correspond to reactions R1, R2, and R3 in Table 1), with and without the inclusion of the tunneling effect. Figure 5 shows the Arrhenius plots for these reactions compared to the experimental results. The discrete symbols correspond to the experimental values, and the lines correspond to the theoretical predictions by means of the CVT/SCT methodology. As explained above and in our previous work,[9,10] the parameters obtained from the application of the genetic algorithm fit the experimental reaction rates for the perprotio reaction. Recall that these parameters ($F_0 = 0.624$, $\gamma = 0.180$ Å, and $\Delta V = -40.18$ kcal/mol) will not be changed for the study of the different KIEs in this work because they only affect the potential energy surface, which, by means of the Born−Oppenheimer approximation, is not changed with the different isotopic substitutions.

In ref 10 we discussed the different trends of the two terms in eq 7 for the addition reaction, and this will not be repeated entirely here. However, it is worthwhile to outline the main observations of that work. If we only use CVT, without inclusion of the tunneling correction, to obtain the rate constants for reactions R1, R2, and R3, the theoretical results are entirely different from those in Figure 5 (see also Figure 1 in ref 10). At low temperatures ($T < 150$ K), the relationship between the CVT reaction rates is $k_D^{CVT} > k_H^{CVT} > k_{Mu}^{CVT}$. At high temperatures, however, the relationship is inverted: $k_{Mu}^{CVT} > k_H^{CVT} > k_D^{CVT}$. This inversion of the relative value of the rate coefficients was noted previously by Nagase et al.,[6] who used conventional transition-state theory without any tunneling correction. A totally different picture is obtained at low temperatures when including the tunneling effect in the calculations. Now, the CVT/MT rate constants are sorted in the same order at all temperatures, being higher for lighter isotopes. This different behavior of reaction rates with and without the inclusion of tunneling can also be seen in Table 7. The slopes of the CVT KIEs as functions of temperature have signs opposite

TABLE 7: Primary Kinetic Isotope Effects on $X + C_2H_4$, with X = H, D, and Mu (Reactions R1, R2, and R3 in Table 1)

	$k_{Mu}/k_H = k_3/k_1$				$k_H/k_D = k_1/k_2$			
T (K)	CVT	CVT/ZCT	CVT/SCT	exptl[a]	CVT	CVT/ZCT	CVT/SCT	exptl[b]
150	0.04	7.1	17.9		1.04	1.79	2.00	
200	0.15	3.0	6.7	17.9[c]	1.14	1.49	1.61	
250	0.34	2.2	4.0	7.1	1.18	1.39	1.45	1.47
300	0.56	2.0	3.2	5.3	1.19[d]	1.32	1.37	1.45
400	0.98	2.0	2.8	3.3	1.23	1.47	1.49	1.43
500	1.33	2.2	2.6		1.28	1.43	1.45	
600	1.61	2.3	2.6		1.30	1.39	1.41	
700	1.82	2.4	2.7		1.30	1.37	1.37	
800	1.96	2.5	2.7		1.30	1.35	1.35	
900	2.08	2.6	2.7		1.30	1.33	1.33	
1000	2.17	2.6	2.7		1.30	1.32	1.32	

[a] References 3 and 4. [b] Reference 3. [c] Extrapolated. [d] Cowfer and Michael (ref 2) obtained 1.32 by conventional transition-state theory with $R^{\ddagger}_{C-X} = 2.10$ Å.

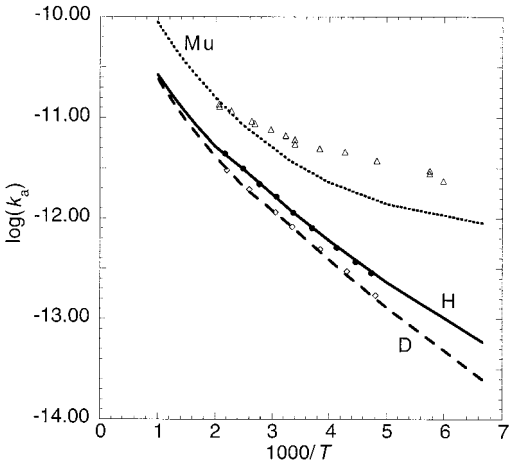

Figure 5. Arrhenius plots for the CVT/SCT calculations (lines) for the $X + C_2H_4$ addition, with X = Mu, H, and D. Also shown are the experimental data: Mu, open triangles;[4] H, solid circles;[3] D, open diamonds.[3] Rate constants are in cm^3 molecule^{-1} s^{-1}.

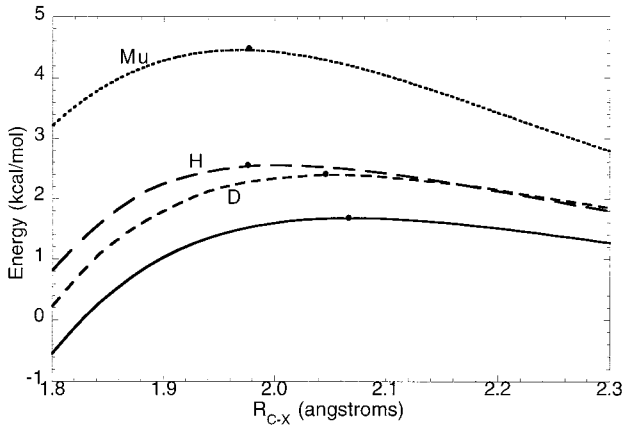

Figure 6. V_M curves (solid lines) and V_a^G curves for X = Mu (dotted line), H (long-dashed line), and D (short-dashed line) as functions of the R_{C-X} distance. The solid circles indicate the location of the maximum of each curve. Although the three reactions have different V_M curves, the differences between them are smaller than the plotting resolution, and thus, the three lines appear superimposed.

those in the corresponding CVT/MT calculations for both the deuterium and the muonium cases. The reason for this behavior is illustrated in Figure 6, which is discussed next.

Figure 6 shows the classical energy profile, $V_M(s)$, and the quantal adiabatic ground-state barrier, $V_a^G(s)$ (defined in eq 3) measured from reactants, as functions of the R_{C-X} distance for the three isotopes. The zero-point-inclusive energy barriers for the addition are 2.63, 2.47, and 4.44 kcal/mol for R1, R2, and R3, respectively. At low temperatures without tunneling, where the height of the zero-point-inclusive energy barrier is the main factor in determining the rate constant, we obtain the relationship $k_D^{CVT} > k_H^{CVT} > k_{Mu}^{CVT}$ in the order expected from the order of the zero-point-inclusive barriers. At high temperatures, the trend is reversed because the dynamics are now dominated by the translational partition function. When the tunneling contribution is included, the behavior at low temperatures changes. Although the barrier is highest for muonium and lowest for deuterium, tunneling through the barrier is an exponentially increasing function of the square root of the appropriate reciprocal mass. Thus, when taking into account the tunneling effect, $k_{Mu}^{CVT/MT} > k_H^{CVT/MT} > k_D^{CVT/MT}$ at all temperatures considered.

Parts a and b of Figure 7 show the evolution of the generalized frequencies along the path for reactions R1 and R3, respectively. Note that the most significant difference is in the value of two lowest frequencies. These correspond to the two bending frequencies associated with the forming C−X bond. Nagase et al. obtained 404 cm^{-1} for the lowest frequency at the saddle point, and Hase et al.[8] obtained 391 cm^{-1}. In contrast, for reaction R1 we obtain 374 cm^{-1} at $s = 0$, and 344, 351, 391, and 417 cm^{-1} at the canonical variational transition states for temperatures of 0, 200, 500, and 1000 K, respectively. These values show that, at least in the middle of the temperature range, our transition state is similar to previous ones, but it also shows a significant temperature dependence for this critical frequency. For reaction R11a, the lowest frequency is 371 cm^{-1} at $s = 0$, and we obtain 341, 348, 393, and 416 cm^{-1} at the variational transitions for 0, 200, 500, and 1000 K, respectively. For reaction R12b the corresponding values are 288, 246, 248, 300, and 307 cm^{-1}. We find similar but slightly smaller variations in the second-lowest frequency. These values illustrate the effect of tightening of the variational transition state as T is raised.

In considering the results in Figure 5 and Table 7, one could argue that the disagreement that still exists between the experimental and theoretical results in the case of the muonium substitution could be due to the large anharmonicity in the muonium case, since anharmonicity has not been included in our calculations. To test this factor, we have used the data calculated in a recent work for the muonium-substituted ethyl radical.[58] Using the data in Table 3 of ref 57, we can calculate the contribution to the zero-point energy of the two bending frequencies in the ethyl radical that are created during the course of the title reaction; these data are given in Table 8. (Note that the C−X stretching mode, which is also created during the addition process, corresponds to the reaction coordinate, and for this reason, it is mostly projected out of the generalized normal-

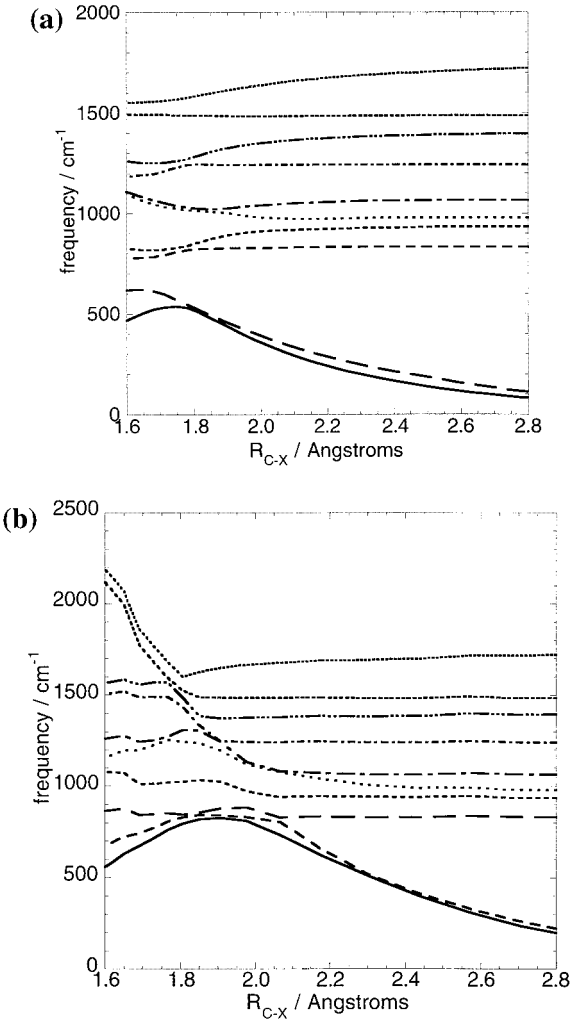

Figure 7. (a) Evolution of the 10 lower generalized frequencies along the reaction path for the H + C_2H_4 addition vs the R_{C-X} distance; (b) the same for the Mu + C_2H_4 addition.

TABLE 8: Contribution of the Transitional Bending Modes to the Zero-Point Energy for Reaction R3

	ZPE (cm^{-1})	
	harm.	anharm.
Product[a]		
C_2H_5	1627	1605
C_2H_4Mu	3773	3608
ZPE(Mu) − ZPE(H)	2146	2003
anharmonicity	0	−143
Transition State		
C_2H_4-H	351[b]	346[c]
C_2H_4-Mu	820[b]	784
ZPE(Mu) − ZPE(H)	469	438
anharmonicity	0	−31[c]

[a] Taken from ref 57. [b] Direct calculation at CVT transition state at 200 K. [c] Assuming same percentage anharmonicity as at products.

mode treatment along the path.) For the product of reaction R1, the contribution to the zero-point energy of the two bending frequencies is 1605 cm^{-1} for the anharmonic treatment and 1627 cm^{-1} for the harmonic one. The contribution in the case of the product of reaction R3 is 3608 cm^{-1} in the anharmonic treatment and 3773 cm^{-1} in the harmonic one. Thus, the difference in the zero-point energy of products between the muonium and the protium addition cases is 2003 cm^{-1} for the anharmonic treatment and 2146 cm^{-1} for the harmonic one. At 200 K this difference of 143 cm^{-1} becomes a factor of 2.77 in the

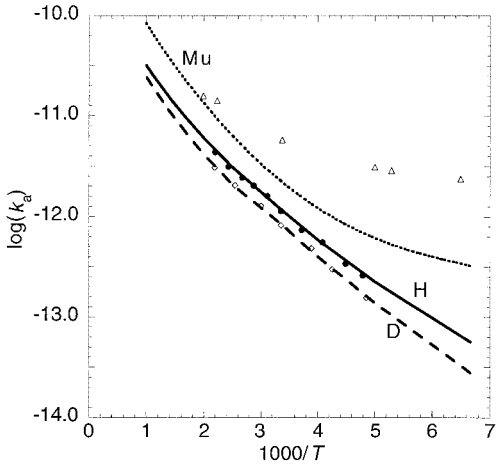

Figure 8. Arrhenius plots for the CVT/SCT calculations (lines) for the X + C_2D_4 addition, with X = Mu, H, and D. Also shown are the experimental data for these reactions: Mu, open triangles;[4] H, solid circles;[3] D, open diamonds.[3] Rate constants are in cm^3 $molecule^{-1}$ s^{-1}.

vibrational partition function of products, favorable to the muonium system. However, this factor is smaller for points along the reaction path where the value of those bending frequencies is smaller than in products. (Note that in reactants those frequencies are not present, and thus, the difference introduced by anharmonicity in the CVT rate constants is due only to the transition-state bending frequencies.) To estimate the effect, we assume the same percentage anharmonicity at the transition state as at products, which is not necessarily true but which is probably more accurate than neglecting anharmonicity. Then, as shown in Table 8, the difference between the muonium and the hydrogen zero-point energy at the transition-state location at 200 K due to the two bending frequencies in our calculations is approximately 31 cm^{-1}. The factor that this difference introduces in the transition-state partition function is only 1.25, which raises the calculated k_{Mu}/k_H from 6.7 to 8.3 but which is clearly is much lower than the ratio between the experimental and the calculated rate constants. Although anharmonicity is significant, it is a smaller effect than tunneling. Tunneling effects for Mu are quantitatively extremely challenging to theory.

In Table 9 we present the results for the primary KIEs for the addition X + C_2D_4, with X = H, D, and Mu (reactions R4, R5, and R6 in Table 1). In Figure 8 we present the Arrhenius plots for these reactions compared to the experimental results. Again, the discrete symbols correspond to experimental data, and the lines correspond to the CVT/SCT calculations. The VSEC parameters predict quite accurate rate coefficients for reactions R4 and R5, and consequently, k_4/k_5 is quite accurate too. The correct trend is also obtained for reaction R6, but in this case, the difference between experiment and theory is bigger than in reaction R3 (see Figure 5 and Table 7). The reason is that the calculated tunneling effect in reaction R6 is much lower than in reaction R3 because of the extremely high sensitivity of this correction to the height of the ΔV_a^G profile in the muonium addition. Thus, while the zero-point-inclusive energy barriers in reactions R4, R5, and R6 (2.53, 2.35, and 4.36 kcal/mol, respectively) are very similar to the values for reactions R1, R2, and R3 (2.63, 2.47, and 4.44 kcal/mol, respectively), the small difference between the ΔV_a^G profiles for reactions R3 and R6 generates a much bigger difference in the tunneling calculations. As a consequence, the primary KIEs for the muonium vs protium additions is 3 times bigger at 150 K for

TABLE 9: Primary Kinetic Isotope Effects on X + C_2D_4, with X = H, D, and Mu (Reactions R4, R5, and R6 in Table 1)

	$k_{Mu}/k_H = k_6/k_4$				$k_H/k_D = k_4/k_5$			
T (K)	CVT	CVT/ZCT	CVT/SCT	exptl[a]	CVT	CVT/ZCT	CVT/SCT	exptl[b]
150	0.04	3.0	5.6		1.03	1.69	2.00	
200	0.16	1.67	2.7	15.6[c]	1.12	1.47	1.61	
250	0.35	1.47	2.0	6.3	1.16	1.37	1.47	1.45
300	0.58	1.49	1.9	5.0	1.19[d]	1.33	1.39	1.41
400	1.02	1.79	2.0	3.6	1.22	1.45	1.49	1.37
500	1.39	2.00	2.2	3.0[c]	1.28	1.43	1.45	
600	1.67	2.2	2.3		1.30	1.39	1.41	
700	1.89	2.4	2.4		1.30	1.35	1.37	
800	2.00	2.4	2.6		1.30	1.33	1.35	
900	2.1	2.5	2.6		1.28	1.32	1.32	
1000	2.2	2.6	2.6		1.28	1.30	1.30	

[a] References 3 and 4. [b] Reference 3. [c] Extrapolated. [d] Cowfer and Michael[2] obtained 1.36 by conventional transition-state theory with $R^{\ddagger}_{C-X} = 2.10$ Å.

TABLE 10: Secondary Kinetic Isotope Effects on H + C_2X_4, with X = H and D (Reactions R1 and R4 in Table 1)

	$k_H/k_D = k_1/k_4$			
T (K)	CVT	CVT/ZCT	CVT/SCT	exptl[a]
150	1.15	1.08	1.14	
200	1.08	1.04	1.09	
250	1.05	1.03	1.05	1.04
300	1.03	1.03	1.04	1.03
400	1.02	1.01	1.02	1.02
500	1.01	1.00	1.00	
600	1.01	0.99	1.00	
700	1.00	0.99	1.00	
800	1.00	0.99	0.99	
900	0.99	0.99	0.99	
1000	0.99	0.99	0.99	

[a] Values taken from ref 3.

TABLE 11: Kinetic Isotope Effects on H + C_2H_3X, with X = H and D (Reactions R1, R8a, and R8b in Table 1)

	$k_1/(k_{8a} + k_{8b})$	
T (K)	CVT/SCT	exptl[a]
150	0.97	
200	0.98	
250	0.99	1.04
300	0.99	1.03
400	0.99	1.02
500	1.00	
600	1.00	
700	1.00	
800	1.01	
900	1.01	
1000	1.01	

[a] Values taken from ref 3.

C_2H_4 at the substrate than for C_2D_4. This will influence some conclusions obtained from the KIEs, as we will see in the next subsection.

The significant underestimation of the tunneling effect for the muonium reactions might be regarded as disappointing. However, the very low mass of the muonium atom, when combined with the unusually low temperatures studied in this paper, makes this kind of calculation an extremely hard test of the theory. It is not clear at this stage of our understanding whether the error is predominantly due to the potential energy surface or to the semiclassical nature of the dynamics calculation. If the former, it is also not clear to what extent the discrepancy is due to the potential along the reaction path and to what extent it is due to the potential characteristics transverse to the path. If the latter (dynamics), it is hard to separate possible errors in the exponential decay of the wave function in the tunneling direction from possible error sources due to the way that quantization is applied to other degrees of freedom, including anharmonicity and mode coupling.

3.4.2. Secondary Kinetic Isotope Effects. Table 10 presents the KIEs for the addition reactions H + C_2X_4, with X = H, D (reactions R1 and R4 in Table 1). The secondary KIEs are close to 1, as usual, and they go from direct (lighter isotope faster) to inverse (lighter isotope slower) as the temperature increases. The tunneling effect does not play an important role in the secondary KIEs at room temperature and above. Table 10 compares the theoretical values of the KIE to the experimental results. It can be seen that the trends are reproduced, and the values for temperatures of 250 K and higher agree very well. At lower temperatures, however, the agreement between theory and experiment is not satisfactory probably because of the difficulty of accurately describing the tunneling at such low temperatures, as pointed out above.

The comparison between the observed and predicted primary and secondary KIEs for the R8 reaction is less satisfactory than the comparison of theory and experiment for R4. The experimental measurements[3] are for the sum of the R8a and R8b and are given in Table 11. Our results disagree with experimental results for the direction of the KIE for R8 in that the calculated $k_1/(k_{8a} + k_{8b})$ (Table 11) is less than unity, although theory agrees that the KIEs approach unity as the temperature increases.

3.4.3. Simultaneous Primary and Secondary KIEs. It is interesting to see if the rule of geometric mean[59−61] (RGM) holds in this system. This rule states that

$$\mathrm{KIE(AB)} = \mathrm{KIE(A)} \times \mathrm{KIE(B)} \tag{12}$$

where A, B, and AB denote respectively deuterium or muonium substitution at position A, position B, and both. This relation may be derived by assuming conventional transition-state theory with no tunneling and no coupling between the motion of substituents at A and B. In other words, this rule expresses the consequence of having independent motion at different locations in the molecule. To test the RGM, we compare the value obtained by using the RGM,

$$\mathrm{KIE_{RGM}(D)} = \frac{k_2}{k_1}\frac{k_4}{k_1} \tag{13}$$

$$\mathrm{KIE_{RGM}(Mu)} = \frac{k_3}{k_1}\frac{k_4}{k_1} \tag{14}$$

with the KIEs obtained by performing double isotopic substitutions, k_5/k_1 and k_6/k_1. The final results are plotted in Figure 9. It is clear than the RGM holds very well for deuterium addition but not for muonium addition. The reason for this breakdown

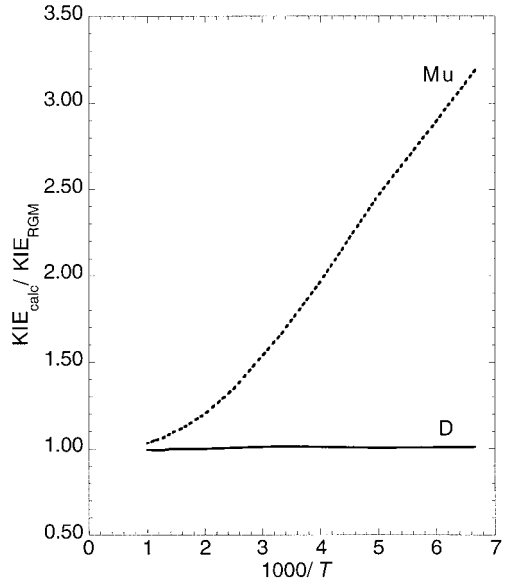

Figure 9. RGM check for the muonium and deuterium additions to C_2H_4 and C_2D_4. KIE_{calc} corresponds to k_1/k_6 for the muonium case and to k_1/k_5 for the deuterium case. KIE_{RGM} corresponds to the product k_3k_4/k_1^2 in the muonium case and to the product k_2k_4/k_1^2 in the deuterium case.

TABLE 12: Kinetic Isotope Effects on D + C_2H_3D (Reactions R10a and R10b in Table 1)

	$k_1/(k_{10a} + k_{10b})$	
T (K)	CVT/SCT	exptl[a]
150	1.92	
200	1.59	
250	1.45	1.39
300	1.35	1.37
400	1.47	1.35
500	1.43	
600	1.39	
700	1.37	
800	1.35	
900	1.33	
1000	1.32	

[a] Values taken from ref 3.

is the large multidimensional tunneling effect present in the muonium case, which involves modes whose coupling affects the results significantly. We confirmed this by testing the RGM by using CVT rate constants with no tunneling correction; in that test the differences between the calculated and the RGM-estimated KIEs are never larger than a 5%. It is also interesting to note that although the final calculations for reaction R5 deviate significantly from experiment (Figure 8), the deviation would be much larger if we used the RGM to predict k_6. This provides an unusual but welcome confirmation of the qualitative correctness of the way modes are coupled in the present multidimensional tunneling calculations. The breakdown of the RGM rule has also been observed by some of the authors in a recent study of tunneling effects in enzymatic reactivity; in that case the RGM breaks down even for D substitution.[62]

In Table 12 we list our calculated $k_1/(k_{10a} + k_{10b})$ ratio, to compare it with another experimentally measured KIE from ref 3. The calculated $k_1/(k_{10a} + k_{10b})$ is in good agreement with experiment for $T \geq 250$ K.

3.4.4. Regioselectivity. In this subsection and the following we present our predictions for positional selectivity and cis−trans effects.

Figure 10 shows the KIEs for the addition of protium to different substrates (reactions R7, R8, and R11 in Table 1). All

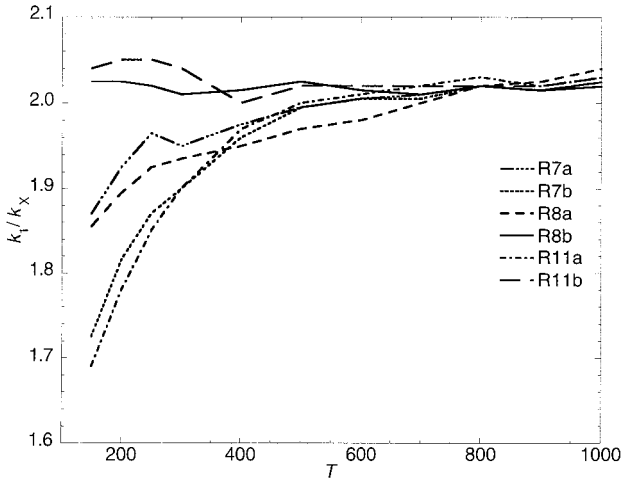

Figure 10. k_1/k_X KIE, where X = 7a, 7b, 8a, 8b, 11a, 11b, as a function of temperature.

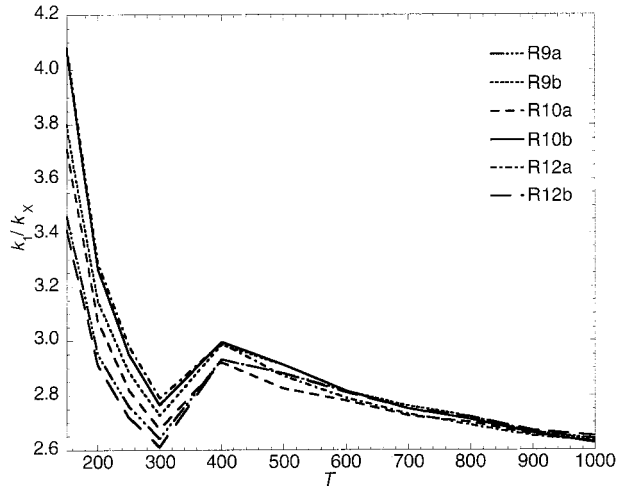

Figure 11. k_1/k_X KIE, where X = 9a, 9b, 10a, 10b, 12a, 12b, as a function of temperature.

KIEs are with respect to reaction R1. The first observation is that at high temperatures the curves approach asymptotically a value that equals the ratio between the σ factors. The different patterns of isotopic substitution show more interesting trends at lower temperatures. After examining the different contributions to the reaction rates, we concluded that the main contribution to the differences in the KIEs for reactions R7, R8, and R11 comes from the vibrational partition function at the transition state. For example, the main factor in the ratio k_{8a}/k_{8b} is the change in the frequencies of the out-of-plane normal modes in the ethylene. Furthermore, k_{8a}/k_{8b} at 150 K is 1.14 at the CVT level and 1.09 at the CVT/SCT level. The small reduction of the ratio due to tunneling is associated with the fact that the zero-point-inclusive energy barrier is slightly higher for reaction R8b than for reaction R8a (2.62 vs 2.58 kcal/mol). Clearly, the final quantitative value of the ratio depends on a delicate balance between tunneling and the vibrational partition functions. Figure 10 shows that at low temperatures protium prefers to add at the most substituted carbon.

Analogously, Figure 11 shows KIEs for the addition of deuterium to different substrates (reactions R9, R10, and R12 in Table 1). In these systems we note how the positional selectivity is stronger at lower temperatures. The large values of the KIE below 200 K are due to the tunneling contribution. The conclusions about the origin of the differences between

reactions R*X*a and R*X*b for $X = 9$, 10, and 12 in Figure 11 are the same as those for $X = 7$, 8, and 11 in Figure 10.

Deuterium also prefers to add to the most substituted position.

The finding that addition to the most substituted carbon is kinetically favored can be compared to the experimental finding in many recent articles[63−65] that substitution occurs at the least substituted position. Several issues need to be considered to put these effects in context. First, we note that the word "substituted" is ambiguous; in this article it refers to replacing H by D. However, when it is compared to replacement of H by a bulkier substituent or a substituent of different electronegativity, it is not clear that this is the correct viewpoint.[66] Consider first steric effects. Melander and Saunders[66] have pointed out that, owing to its wider zero-point motion, the vibrational probability distribution of a carbon−protium oscillator is wider and more space-demanding than that of a carbon−deuterium oscillator. Thus, for steric effects it would not be at all surprising if protium sites (CH_2) play the role of substituted sites and deuterium sites (CD_2) play the role of unsubstituted sites (with the same considerations for CHD vs CD_2 or CH_2 vs CHD). Inductive effects are more complicated and not totally separable from steric effects, but deuterium substitution for protium leads to effects very similar to those of lowering the electronegativity of a substituent by a minute amount.[66] If inductive effects are dominant, then deuterium substitution should correlate with electron-donating substitution (like alkylation) but not with electron-withdrawing substitution (like halogenation). Electromeric effects presents additional complications. Thus, the regioselective directing powers of deuterium substitution can be straightforwardly compared to other substituent effects on regioselectivity only when the dominant factor controlling the direction of the effect has been identified. The discussion earlier in this section shows that the bending vibrations are critical to the direction of the effect in the present case.

3.4.5. Stereoselectivity. The last KIE considered in the present work is the preference for addition to either the cis or trans isomers of CHDCHD (reactions R13−R16 in Table 1). To test this preference, we have calculated the ratios k_{13}/k_{14} and k_{15}/k_{16}. Both ratios are approximately 1 at all temperatures, indicating no special preference for the addition to cis or trans isomers of the ethylene molecule.

4. Concluding Remarks

The present calculations were made possible by several recent advances in the methods for direct dynamics calculations. The calculation of the reaction path and reaction-path Hessians at the QCISD/6-311G(d,p) level was facilitated by using a distinguished-coordinate path (DCP), which allows much larger step sizes than a minimum-energy path (MEP). The use of a DCP for dynamics calculations (determination of the least recrossed dividing surface and multidimensional tunneling calculation including reaction-path curvature) is made possible by the reorientation of the dividing surface (RODS) algorithm. The RODS algorithm also allows one to carry out dynamics calculations for all isotopic variations of the reaction, ranging from Mu to D (a factor of 17.6 in mass) from a single mass-independent reaction path with a single set of mass-independent Hessians. Redundant internal coordinates have been used to define curved generalized-transition-state dividing surfaces; this yields physical frequencies for the generalized normal modes transverse to the reaction path. The various directly calculated reaction-path quantities were interpolated by the recently developed mapped interpolated variational transition-state theory (IVTST-M) algorithm based on a spline under tension along a physically mapped reaction coordinate. All these capabilities are available in version 7.9 of the *Polyrate* code, and the present application provides a good example of how powerful they are when used in concert. Furthermore, these dynamics calculations were combined with the recently developed variable scaling of external correlation (VSEC) procedure for scaling the correlation energy in order to make the energy profile along the reaction path more accurate than could be obtained with unscaled calculations.

The new methods have drastically reduced the number of electronic structure calculations required for calculating rate constants and kinetic isotope effects, and therefore, these calculations can be carried out at very high ab initio or semiempirical levels. In the present work we have demonstrated these techniques by the study of several isotopic substitutions in the $H + C_2H_4$ free radical addition reaction. Comparison of calculated kinetic isotope effects (KIEs) to experimental results allows one to test and to validate the aspects of the implicit potential energy surface to which the results considered here are sensitive. Appropriately validated models may be used to make predictions about the rates of reactions not measured experimentally. Canonical variational transition-state theory with multidimensional semiclassical tunneling calculations has been shown to provide a very useful tool for such studies.

The results show that the importance of the tunneling effect for the primary kinetic isotope effects and reaction rates increases in the series deuterium−protium−muonium. The secondary kinetic isotope effects are close to unity, varying from normal at low temperatures to inverse at higher temperatures. We have found that the rule of the geometric mean (RGM) is approximately satisfied for D but not for Mu.

We have also studied the regioselectivity and stereoselectivity of the addition process. We have found that addition at the more substituted carbon is more favorable for both hydrogen and deuterium, especially at low temperatures. On the other hand, no special preference has been found for the addition to *cis* or *trans* isomers of the isotopically substituted ethylene molecule.

Acknowledgment. The authors are grateful to Patton L. Fast for his comments and suggestions and to Philip Pechukas for helpful discussions. J. V. and J. C. C. acknowledge Virginia P. Trader for her personal support. J. C. C. also acknowledges the Spanish Ministerio de Educación y Cultura and the Fulbright Commission for a postdoctoral scholarship. This work was supported in part by the U.S. Department of Energy, Office of Basic Energy Sciences.

References and Notes

(1) (a) Pilling, M. J. In *Modern Gas Kinetics*; Pilling, M. J., Smith, I. W. M., Eds.; Blackwell Scientific: Oxford, 1987; p 330. (b) Davies, J. W.; Pilling, M. J. *Adv. Gas-Phase Photochem. Kinet.* **1989**, *2*, 105. (c) Lin, M. C.; Back, M. H. *Can. J. Chem.* **1996**, *44*, 505. (d) Lin, M. C.; Back, M. H. *Can. J. Chem.* **1966**, *44*, 505. (e) Loucks, L. F.; Laidler, K. J. *Can. J. Chem.* **1967**, *45*, 2795. (f) Braun, W.; Lenzi, M. *Discussions Faraday Soc.* **1967**, *44*, 252. (g) Westenberg, A. A.; deHaas, N. *J. Chem. Phys.* **1969**, *50*, 707. (h) Kurylo, M. J.; Peterson, N. C.; Braun, W. *J. Chem. Phys.* **1970**, *53*, 2776. (i) Eyre, J. A.; Hikida, T.; Dorfman, L. *J. Chem. Phys.* **1970**, *53*, 1281. (j) Barker, J. R.; Keil, D. G.; Michael, J. V.; Osborne, D. T. *J. Chem. Phys.* **1970**, *52*, 2079. (k) Michael, J. V.; Cowfer, J. A.; Keil, D. G.; Yeh, C. *J. Phys. Chem.* **1971**, *75*, 1584. (l) Michael, J. V.; Osborne, D. T.; Suess, G. N. *J. Chem. Phys.* **1973**, *58*, 2300. (m) Jones, W. E.; Macknight, S. D.; Teng, L. *Chem. Rev.* **1973**, *73*, 407. (n) Lee, J. H.; Michael, J. V.; Payne, W. A.; Stief, L. J. *J. Chem. Phys.* **1978**, *68*, 1817. (o) Oka, K.; Cvetanović, R. J. *Can. J. Chem.* **1979**, *57*, 777. (p) Pacey, P. D.; Wimalasena, J. H. *Chem. Phys. Lett.* **1980**, *76*, 433. (q) Pacey, P. D.; Wimalasena, J. H. *J. Phys. Chem.* **1984**, *88*, 5657. (r) Trenwith, A. B. *J. Chem. Soc., Faraday Trans.* **1986**, *82*, 457. (s) Lightfoot, P. D.; Pilling, M. J. *J. Phys. Chem.* **1987**, *91*, 3373. (t) Simon, Y.; Foucaut, J. F.; Scacchi, G. *Can. J. Chem.* **1988**, *66*, 2142. (u) Hanning-Lee, M. A.; Green, N. J. B.; Pilling, M. J.; Robertson, S. H. *J. Phys. Chem.* **1993**, *97*, 860. (v) Feng, Y.; Niiranen, J. T.; Bencsura, Á., Knyazev, V. D.; Gutman, D.; Tsang, W. *J. Phys. Chem.* **1993**, *97*, 871.

(2) Cowfer, J. A.; Michael, J. V. *J. Chem. Phys*. **1975**, *62*, 3504.
(3) (a) Sugawara, K.; Okazaki, K.; Sato, S. *Chem. Phys. Lett*. **1981**, *78*, 259. (b) Sugawara, K.; Okazaki, K.; Sato, S. *Bull. Chem. Soc. Jpn.* **1981**, *54*, 2872.
(4) Garner, D. M.; Fleming, D. G.; Arseneau, D. J.; Senba, M.; Reid, I. D.; Mikula, R. J. *J. Chem. Phys*. **1990**, *93*, 1732.
(5) (a) Michael, J. V.; Suess, G. N. *J. Chem. Phys*. **1973**, *58*, 2807. (b) Sloane, C.; Hase, W. L. *Faraday Discuss. Chem. Soc*. **1977**, *62*, 210. (c) Hase, W. L.; Mrowka, G.; Brudzynski, R.; Sloane, C. S. *J. Chem. Phys*. **1978**, *69*, 3548. (d) Hase, W. L.; Wolf, R. J.; Sloane, C. S. *J. Chem. Phys*. **1979**, *71*, 2911. (e) Hase, W. L.; Mrowka, G.; Brudzynski, R.; Sloane, C. S. *J. Chem. Phys*. **1980**, *72*, 6321. (f) Hase, W. L.; Ludlow, D. M.; Wolf, R. J.; Schlick, T. *J. Phys. Chem*. **1981**, *85*, 958. (g) Schlegel, H. B. *J. Phys. Chem*. **1982**, *85*, 4878. (h) Hase, W. L.; Buckowski, D. G. *J. Comput. Chem*. **1982**, *3*, 335. (i) Hase, W. L.; Schlegel, H. B. *J. Phys. Chem*. **1982**, *86*, 3901. (j) Hase, W. L.; Buckowski, D. G.; Swamy, K. N. *J. Phys. Chem*. **1983**, *87*, 2754. (k) Swamy, K. N.; Hase, W. L. *J. Phys. Chem*. **1983**, *87*, 4715. (l) Sosa, C.; Schlegel, H. B. *Int. J. Quantum Chem*. **1986**, *29*, 1001. (m) Mole, S. J.; Zhou, X.; Liu, R. *J. Phys. Chem*. **1996**, *100*, 14665. (n) Nguyen, M. T.; Creve, S.; Vanquickenborne, L. G. *J. Phys. Chem*. **1996**, *100*, 18422. (o) Jursic, B. S. *J. Chem. Soc., Perkin Trans. 2* **1997**, *637*.
(6) Nagase, S.; Fueno, T.; Morokuma, K. *J. Am. Chem. Soc*. **1979**, *101*, 5849. Additional details of this calculation are published in ref 3a.
(7) (a) Schlegel, H. B. *J. Phys. Chem*. **1982**, *86*, 4878. (b) Schlegel, H. B.; Bhalla, K. C.; Hase, W. L. *J. Phys. Chem*. **1982**, *86*, 4883.
(8) Hase, W. L.; Schlegel, H. B.; Balbyshev, V.; Page, M. *J. Phys. Chem*. **1996**, *100*, 5354; **1997**, *101*, 5026 (E).
(9) Villà, J.; González-Lafont, A.; Lluch, J. M.; Truhlar, D. G. *J. Am. Chem. Soc*. **1998**, *120*, 5559.
(10) Villà, J.; Corchado, J. C.; González-Lafont, A.; Lluch, J. M.; Truhlar, D. G. *J. Am. Chem. Soc*. **1998**, *120*, 12141.
(11) Bradley, J. N.; Melville, H. W.; Robb, J. C. *Proc. R. Soc. A* **1956**, *236*, 318.
(12) (a) Schlegel, H. B. *J. Chem. Phys*. **1986**, *84*, 4530. (b) Gonzalez, C.; Sosa, C.; Schlegel, H. B. *J. Phys. Chem*. **1989**, *93*, 2435, 8388 (E). (c) Barone, V.; Orlandini, L. *Chem. Phys. Lett*. **1995**, *246*, 45. (d) Wong, M.; Radom, L. *J. Phys. Chem*. **1995**, *99*, 8582.
(13) Mayer, P. M.; Parkinson, C.; Smith, D. M.; Radom, L. *J. Chem. Phys*. **1998**, *108*, 604.
(14) Villà, J.; González-Lafont, A.; Lluch, J. M.; Corchado, J. C.; Espinosa-García, J. *J. Chem. Phys*. **1997**, *107*, 7266.
(15) Garrett, B. C.; Truhlar, D. G.; Melius, C. F. *Phys. Rev. A* **1981**, *24*, 2853.
(16) (a) Brown, F. B.; Truhlar, D. G. *Chem. Phys. Lett.* **1985**, *117*, 307. (b) For a review, see the following. Corchado, J. C.; Truhlar, D. G. *ACS Symp. Ser*. **1998**, *712*, 106.
(17) (a) Truhlar, D. G.; Garrett, B. C. *Annu. Rev. Phys. Chem*. **1984**, *35*, 159. (b) Truhlar, D. G.; Isaacson, A. D.; Garrett, B. C. In *Theory of Chemical Reaction Dynamics*; Baer, M., Ed.; CRC Press: Boca Raton, FL, 1985; Vol. 4, p 65. (c) Tucker, S. C.; Truhlar, D. G. In *New Theoretical Concepts for Understanding Organic Reactions*; Bertrán, J., Csizmadia, I. G., Eds.; Kluwer: Dordrecht, 1989.
(18) Truhlar, D. G. In *The Reaction Path in Chemistry*; Heidrich, D., Ed.; Kluwer Academic: Dordrecht, 1995; p 229.
(19) Shavitt, I. *J. Chem. Phys.* **1968**, *49*, 4048.
(20) (a) Truhlar, D. G.; Kuppermann, A. *J. Am. Chem. Soc.* **1971**, *93*, 1840. (b) Truhlar, D. G.; Kuppermann, A. *J. Chem. Phys.* **1972**, *56*, 2232. (c) Garrett, B. C.; Truhlar, D. G. *J. Phys. Chem.* **1979**, *83*, 1079; **1983**, *87*, 4553 (E).
(21) (a) Fukui, K. In *The World of Quantum Chemistry*; Daudel, R., Pullman, B., Eds.; Reidel: Dordrecht, 1974; p 113. (b) Fukui, K. *Pure Appl. Chem.* **1982**, *54*, 1825.
(22) Villà, J.; Truhlar, D. G. *Theor. Chem. Acc*. **1997**, *97*, 317.
(23) (a) Fast, P. L.; Truhlar, D. G. *J. Chem. Phys*. **1998**, *109*, 3721. (b) Fast, P. L.; Corchado, J. C.; Truhlar, D. G. *J. Chem. Phys.* **1998**, *109*, 6237.
(24) González-Lafont, A.; Villà, J.; Lluch, J. M.; Bertrán, J.; Steckler, R.; Truhlar, D. G. *J. Phys. Chem. A* **1998**, *102*, 3420.
(25) (a) Rothman, M. J.; Lohr, L. L., Jr.; Ewing, C. S.; van Wazer, J. R. In *Potential Energy Surfaces and Dynamics Calculations*; Truhlar, D. G., Ed.; Plenum: New York, 1981; p 653. (b) Steckler, R.; Truhlar, D. G. *J. Chem. Phys.* **1990**, *93*, 6570. (c) Heidrich, D. In *The Reaction Path in Chemistry*; Heidrich, D., Ed.; Kluwer: Dordrecht, 1995.
(26) Frisch, M. J.; Trucks, G. W.; Schlegel, H. B.; Gill, P. M. W.; Johnson, B. G.; Robb, M. A.; Cheeseman, J. R.; Keith, T. A.; Petersson, G. A.; Montgomery, J. A.; Raghavachari, K.; Al-Laham, M. A.; Zakrzewski, V. G.; Ortiz, J. V.; Foresman, J. B.; Cioslowski, J.; Stefanov, B. B.; Nanayakkara, A.; Challacombe, M.; Peng, C. Y.; Ayala, P. Y.; Chen, W.; Wong, M. W.; Andres, J. L.; Replogle, E. S.; Gomperts, R.; Martin, R. L.; Fox, D. J.; Binkley, J. S.; Defrees, D. J.; Baker, J.; Stewart, J. J. P.; Head-Gordon, M.; Gonzalez, C.; Pople, J. A. *Gaussian 94*; Gaussian, Inc.: Pittsburgh, PA, 1995.
(27) Hehre, W. J.; Radom, L.; Schleyer, P. v. R.; Pople, J. A. In *Ab Initio Molecular Orbital Theory*; Wiley: New York, 1986.
(28) Pople, J. A.; Head-Gordon, M.; Raghavachari, K. *J. Chem. Phys.* **1987**, *87*, 5968.
(29) Garrett, B. C.; Truhlar, D. G. *J. Chem. Phys.* **1979**, *70*, 1593.
(30) (a) Jackels, C. F.; Gu, Z.; Truhlar, D. G. *J. Chem. Phys.* **1995**, *102*, 3188. (b) Chuang, Y.-Y.; Truhlar, D. G. *J. Chem. Phys.* **1997**, *107*, 83.
(31) Miller, W. H.; Handy, N. C.; Adams, J. E. *J. Chem. Phys*. **1980**, *72*, 99.
(32) Isaacson, A. D.; Truhlar, D. G. *J. Chem. Phys.* **1982**, *76*, 1380.
(33) Truhlar, D. G.; Isaacson, A. D.; Skodje, R. T.; Garrett, B. C. *J. Phys. Chem*. **1982**, *86*, 2252.
(34) Lu, D.-h.; Truong, T. N.; Melissas, V. S.; Lynch, G. C.; Liu, Y.-P.; Garrett, B. C.; Steckler, R.; Isaacson, A. D.; Rai, S. N.; Hancock, G. C.; Lauderdale, J. G.; Joseph, T.; Truhlar, D. G. *Comput. Phys. Commun*. **1992**, *71*, 235.
(35) Liu, Y.-P.; Lynch, G. C.; Truong, T. N.; Lu, D.-h.; Truhlar, D. G.; Garrett, B. C. *J. Am. Chem. Soc*. **1993**, *115*, 2408.
(36) (a) Cízek, J. *J. Chem. Phys.* **1966**, *45*, 4256. (b) Purvis, G. D.; Bartlett, R. J. *J. Chem. Phys.* **1982**, *76*, 1910. (c) Scuseria, G. E.; Janssen, C. L.; Schaefer, H. F., III *J. Chem. Phys.* **1989**, *89*, 7382.
(37) Raghavachari, K.; Trucks, G. W.; Pople, J. A.; Head-Gordon, M. *Chem. Phys. Lett.* **1989**, *157*, 479.
(38) (a) Roos, B. O.; Taylor, P. R.; Siegbahn, P. E. M. *Chem. Phys*. **1980**, *48*, 152. (b) Mok, D. K. W.; Neumann, R.; Handy, N. C. *J. Phys. Chem.* **1996**, *100*, 6225.
(39) McDouall, J. J. W.; Peasley, K.; Robb, M. A. *Chem. Phys. Lett.* **1988**, *148*, 183.
(40) Chen, Z. *Theor. Chim. Acta* **1989**, *75*, 481.
(41) Pechukas, P. *Annu. Rev. Phys. Chem*. **1981**, *32*, 159.
(42) Pechukas, P. *J. Chem. Phys.* **1976**, *64*, 1516.
(43) Irikura, K. K. *ACS Symp. Ser.* **1998**, *677*, 402.
(44) Truhlar, D. G. *J. Comput. Chem.* **1992**, *12*, 266.
(45) Corchado, J. C.; Coitiño, E. L.; Chuang, Y.-Y.; Fast, P.; Truhlar, D. G. *J. Phys. Chem. A* **1998**, *102*, 2424.
(46) Corchado, J. C.; Chuang, Y.-Y.; Fast, P.; Villà, J.; Coitiño, E. L.; Hu, W.-P.; Liu, Y.-P.; Lynch, G. C.; Nguyen, K. A.; Jackels, C. F.; Gu, M. Z.; Rossi, I.; Clayton, S.; Melissas, V. S.; Steckler, R.; Garrett, B. C.; Isaacson, A. D.; Truhlar, D. G. *Polyrate*, version 7.9; University of Minnesota: Minneapolis, MN, 1998; p 185.
(47) Shavitt, I. In *Advanced Theories and Computational Approaches to the Electronic Structure of Molecules*; Dykstra, C. E., Ed.; Reidel: Boston, 1984.
(48) (a) Pauling, L. *J. Am. Chem. Soc*. **1947**, *69*, 542. (b) Johnston, H. S.; Parr, C. A. *J. Am. Chem. Soc.* **1963**, *85*, 2544. (c) Truhlar, D. G. *J. Am. Chem. Soc.* **1972**, *94*, 7584.
(49) (a) Morse, P. M. *Phys. Rev*. **1929**, *34*, 57. (b) Johnston, H. S. *Adv. Chem. Phys*. **1960**, *3*, 131.
(50) (a) Burton, P. G.; Buenker, R. J.; Bruna, P. J.; Peyerimhoff, S. D. *Chem. Phys. Lett.* **1983**, *95*, 379. (b) Bauschlicher, C. W., Jr.; Taylor, P. R. *J. Chem. Phys.* **1987**, *86*, 858. (c) Shavitt, I.; Brown, F. B.; Burton, P. G. *Int. J. Quantum Chem.* **1987**, *31*, 507.
(51) (a) Böhme, M.; Frenking, G. *Chem. Phys. Lett.* **1994**, *224*, 195. (b) Rodríguez-Santiago, L.; Branchadell, V.; Sodupe, M. *J. Chem. Phys.* **1995**, *103*, 9738.
(52) Rossi, I.; Truhlar, D. G. *Chem. Phys. Lett.* **1995**, *233*, 64.
(53) Carroll, D. L. *GA*, version 1.6.4; University of Illinois at Urbana−Champaign, Urbana, IL, 1997.
(54) Duncan, J. L. *Mol. Phys.* **1974**, *28*, 1177.
(55) (a) Hammond, G. S. *J. Am. Chem. Soc.*. **1955**, *77*, 334. (b) Parr, C. A.; Truhlar, D. G. *J. Phys. Chem*. **1971**, *75*, 1844.
(56) See, for example, the following reference. Durant, J. L. *ACS Symp. Ser*. **1998**, *677*, 267.
(57) (a) Lee, T. J.; Rice, J. E.; Scuseria, G. E.; Schaefer, H. F. *Theor. Chim. Acta* **1989**, *75*, 81. (b) Lee, T. J.; Taylor, P. R. *Int. J. Quantum Chem.* **1989**, *23*, 199.
(58) Webster, B.; Buttar, D. *J. Chem. Soc., Faraday Trans.* **1996**, *92*, 2331.
(59) Bigeleisen, J. *J. Chem. Phys.* **1955**, *23*, 2264.
(60) Villà, J.; González-Lafont, A.; Lluch, J. M. *J. Phys. Chem.* **1996**, *100*, 19398.
(61) (a) Klinman, J. P. In *Enzyme Mechanisms from Isotope Effects*; Cook, P. F., Ed.; CRC Press: Boca Raton, FL, 1991; Chapter 4. (b) Amin, M.; Price, R. C.; Saunders: W. H., Jr. *J. Am. Chem. Soc.* **1993**, *115*, 14.
(62) Alhambra, C.; Gao, J.; Corchado, J. C.; Villà, J.; Truhlar, D. G. *J. Am. Chem. Soc.*, in press.
(63) Chandra, A. K.; Nguyen, M. T. *J. Chem. Soc., Perkin Trans. 2* **1997**, 1415.
(64) Zytowski, T.; Fischer, H. *J. Am. Chem. Soc*. **1997**, *119*, 12869.
(65) Sekusak, S.; Liedl, K. R.; Sabljic, A. *J. Phys. Chem. A* **1998**, *102*, 1583.
(66) Melander, L.; Saunders: W. H., Jr. *Reaction Rates of Isotopic Molecules*, 2nd ed.; John Wiley & Sons: New York, 1980; Chapter 6.